

A Hermite Method with a Discontinuity Sensor for Hamilton-Jacobi Equations

Allen Alvarez Loya · Daniel Appelö

Received: date / Accepted: date

Abstract We present a Hermite interpolation based partial differential equation solver for Hamilton-Jacobi equations. Many Hamilton-Jacobi equations have a nonlinear dependency on the gradient of the solution, which gives rise to discontinuities in the gradient of the solution, resulting in kinks in the solution itself. We built our solver with two goals in mind: 1) high order accuracy in smooth regions and 2) sharp resolution of kinks. To achieve this, we use Hermite interpolation with a smoothness sensor. The degrees-of-freedom of Hermite methods are tensor-product Taylor polynomials of degree m in each coordinate direction. The method uses $(m + 1)^d$ degrees of freedom per node in d -dimensions and achieves an order of accuracy $(2m + 1)$ when the solution is smooth. To obtain sharp resolution of kinks, we sense the smoothness of the solution on each cell at each timestep. If the solution is smooth, we march the interpolant forward in time with no modifications. When our method encounters a cell over which the solution is not smooth, it introduces artificial viscosity locally while proceeding normally in smooth regions. We show through numerical experiments that the solver sharply captures kinks once the solution loses continuity in the derivative while achieving $2m + 1$ order accuracy in smooth regions.

Keywords Hermite method · high order · Hamilton Jacobi

AAL was supported by NSF Grant DGE-1650115. DA was supported, in part, by NSF Grant DMS-1913076. Any opinions, findings, and conclusions or recommendations expressed in this material are those of the authors and do not necessarily reflect the views of the National Science Foundation

Allen Alvarez Loya
Department of Applied Mathematics, University of Colorado at Boulder
Engineering Center, ECOT 225
526 UCB
Boulder, CO 80309-0526
Tel.: 714-864-0760
E-mail: allen.alvarezloya@colorado.edu

Daniel Appelö
Department of Computational Mathematics, Science & Engineering and Department of Mathematics, Michigan State University, East Lansing, USA.
E-mail: appeloda@msu.edu

1 Introduction

We consider the time-dependent Hamilton-Jacobi (HJ) equation

$$\varphi_t + H(\varphi_{x_1}, \varphi_{x_2}, \dots, \varphi_{x_d}) = 0, \quad \varphi(\mathbf{x}, 0) = \varphi^0(\mathbf{x}), \quad \mathbf{x} \in \Omega \in \mathbb{R}^d, \quad (1)$$

with periodic boundary conditions on $\partial\Omega$. HJ equations appear in many applications, e.g., optimal control, differential games, image processing and the calculus of variations. The solution of an HJ equation may develop a discontinuity in the derivative even when the initial data is smooth. As for conservation laws the unique solution can be singled out by the use of viscosity solutions [7, 5]. In particular, the viscosity solution gives requirements on the solution at points of discontinuity that allow us to find the unique physically relevant solution. Design of methods for HJ equations that: a) converge to the viscosity solution as the grid is refined even in the presence of kinks, and b.) maintain high-order accuracy in smooth regions and here we only mention a few. The first methods to try to accomplish this were introduced in [22, 6]. Essentially non-oscillatory (ENO) [18] or weighted ENO (WENO) [14, 25] have been developed to solve the HJ equation. These methods have been shown to work efficiently, but require a large stencil size in order to obtain high-order accuracy. More recently, there has been work done by using discontinuous Galerkin methods to solve conservation laws. This idea was introduced in [18], where the authors exploited the fact that the gradient of the solution satisfies a conservation law system, and used a standard discontinuous Galerkin method to advance the solution in time and then recovered the solution from the derivatives. In reference [3] the authors developed a discontinuous Galerkin method for directly solving (1), when the Hamiltonian is linear or convex, this eliminates the need to solve systems in the multidimensional case. This work was later improved upon in [4]. The improvement extends the method to approximate solutions to (1) when the Hamiltonian is not convex. Other improvements include avoiding reconstruction of the solution across elements by utilizing the Roe speed at the cell interfaces and adding an entropy fix inspired by Harten and Hyman [13].

In [21] Qiu and Shu use WENO methods together with Hermite interpolating polynomials (HWENO). These methods are derived from the original WENO methods, but both the function and the first derivative are evolved and used in the reconstruction of the solution. An important advantage of HWENO over WENO is that a more compact stencil may be used for the same order of accuracy. There have been several expansions on this work [20, 26, 23, 24], where in [24] the authors develop a seventh order method, which is the same order of accuracy we obtain using three derivatives. The success of HWENO methods has inspired us to build a Hermite method solver for (1). Using Hermite methods, we may achieve an arbitrary order while keeping a compact stencil.

Hermite methods were first studied in [9], where the authors use Hermite methods to solve hyperbolic initial-boundary value problems. Stability of the method and convergence was proved and various numerical examples were provided. There have been several papers since then that use variants of the original Hermite method. In [1] the authors use Hermite interpolants to solve the wave equation using dissipative and conservative formulations. A hybrid Hermite-discontinuous Galerkin method was used in [2], where the authors approximated the solution of Maxwell's equations. In [16] Hermite methods for hyperbolic conservation laws

were considered, where the entropy viscosity by Guermond et al., [10], was adopted to the Hermite framework. The current paper presents the first Hermite method for Hamilton-Jacobi equations.

The challenge in solving Hamilton-Jacobi equations stems from the nonlinear dependency on the gradient of the solution, which gives rise to discontinuities in the gradient of the solution, resulting in kinks in the solution itself. To resolve the kinks, we sense the smoothness of the solution on each cell at each timestep by adopting the sensor introduced by Persson and Peraire in [19] and later refined by Klockner, Warburton and Hesthaven in [15]. Following [19, 15] we make no modifications if the solution is smooth but when the solution fails to be smooth we locally introduce artificial viscosity. Through numerical experiments we demonstrate that the solver has the following properties: 1) high order accuracy in smooth regions and 2) sharp resolution of kinks.

The rest of this paper is organized as follows: in Section 2 we introduce the numerical scheme for the one-dimensional and two-dimensional HJ equations. Section 3 explains how we sense the smoothness of each element. Section 4 is devoted to the discussion of numerical experiments. Conclusions and future work are discussed in Section 5.

2 Hermite Methods

A Hermite method of order $2m+1$ approximates the solution to a PDE by element-wise polynomials that interpolate the solution and derivatives up to degree m at the element interfaces. The time evolution is done locally from the center of the element. In Hermite methods, the degrees of freedom are the function and the spatial derivatives, or equivalently the Taylor coefficients. The evolution of the polynomials depends on the nature of the PDE.

2.1 Hermite Method in One Dimension

We describe a Hermite PDE method in one-dimension for HJ equations. This method closely follows the Hermite solver for conservation laws described in [12]. Note that we use this method, with no modifications, while the solution is smooth. Consider the Hamilton-Jacobi equation, with periodic boundary conditions

$$u_t = \begin{cases} \varphi_t + H(\varphi_x) = 0, \\ \varphi(x, 0) = \varphi^0(x). \end{cases} \quad (2)$$

2.1.1 Initialization

We discretize the spatial coordinate into a primal grid and a dual grid

$$x_i = x_l + ih_x, \quad h_x = (x_r - x_l)/n_x, \quad (3)$$

where $i = 0, \dots, n_x$ for the primal grid and $i = 1/2, \dots, n_x - 1/2$ for the dual grid. The first step initializes the degrees of freedom by setting them to be the scaled

derivatives at each primal grid point. That is,

$$c_{l,i} = \frac{h_x^l}{l!} \left. \frac{d^l u(x,0)}{dx^l} \right|_{x=x_i}.$$

We then interpolate scaled derivative data to obtain the piecewise degree- $2m+1$ polynomial

$$v_{i+\frac{1}{2}}(x,0) = \sum_{l=0}^{2m+1} d_{l,i+\frac{1}{2}} \left(\frac{x - x_{i+\frac{1}{2}}}{h_x} \right)^l, \quad (4)$$

where the coefficients $d_{l,i}$ are uniquely determined by the interpolation conditions

$$\frac{h_x^l}{l!} \frac{\partial^l}{\partial x^l} v_{i+\frac{1}{2}}(x_i) = c_{l,i}, \quad \frac{h_x^l}{l!} \frac{\partial^l}{\partial x^l} v_{i+\frac{1}{2}}(x_{i+1}) = c_{l,i+1}, \quad (5)$$

for $l = 0, \dots, m$.

2.1.2 Evolution

We treat the coefficients in the Hermite interpolant as functions of time. That is,

$$v_{i+\frac{1}{2}}(x,t) = \sum_{l=0}^{2m+1} d_{l,i+\frac{1}{2}}(t) \left(\frac{x - x_{i+\frac{1}{2}}}{h_x} \right)^l. \quad (6)$$

For our PDE $\varphi_t = -H(\varphi_x)$ we substitute (6):

$$\frac{\partial v_{i+\frac{1}{2}}(x,t)}{\partial t} = \sum_{l=0}^{2m+1} d'_{l,i+\frac{1}{2}}(t) \left(\frac{x - x_{i+\frac{1}{2}}}{h_x} \right)^l = -H(v_x(x,t)). \quad (7)$$

We can differentiate (7) k times in space and evaluate at $x = x_{i+\frac{1}{2}}$ to obtain

$$\frac{k!}{h_x^k} d'_{k,i+\frac{1}{2}}(t) = - \left. \frac{\partial^k}{\partial x^k} H(v_x(x,t)) \right|_{x=x_{i+\frac{1}{2}}}. \quad (8)$$

When H is nonlinear the differentiation of the RHS can spawn new terms by the product rule. We avoid this by approximating the RHS by a Taylor polynomial of degree $2m+1$

$$H(v_x) \approx \sum_{l=0}^{2m+1} b_{l,i+\frac{1}{2}}(t) \left(\frac{x - x_{i+\frac{1}{2}}}{h_x} \right)^l. \quad (9)$$

for which the differentiation is straight forward. With this approximation we carry out the differentiation in (8) we obtain the local system of ODEs

$$d'_{k,i+\frac{1}{2}}(t) = b_{k,i+\frac{1}{2}}(t), \quad k = 0, \dots, 2m+1. \quad (10)$$

We can solve this system to evolve our approximate solution using a standard one step ODE solver as described in [11]. Before we evolve we must find the Taylor coefficients $b_{k,i+\frac{1}{2}}(t)$. The computation of the coefficients, $b_{k,i+\frac{1}{2}}$, is problem specific and depends on the form of the Hamiltonian, H .

2.1.3 Polynomial Approximation of Non-linear Hamiltonians

We describe this process for the PDE that is used in example 3 in the numerical experiments section below

$$\varphi_t = \cos(\varphi_x + 1).$$

A Taylor series expansion for the right hand side of this equation can be obtained by techniques from automated differentiation. If in general the functions $f(x)$, $w(x)$ and $u(x)$ have Taylor series expansions

$$\begin{aligned} f(x) &= \sum_{k=0}^{\infty} F_k \left(\frac{x - x_i}{h} \right)^k, \\ w(x) &= \sum_{k=0}^{\infty} W_k \left(\frac{x - x_i}{h} \right)^k, \\ u(x) &= \sum_{k=0}^{\infty} U_k \left(\frac{x - x_i}{h} \right)^k, \end{aligned}$$

then for non-linearities that satisfy a differential equation $f'(x) = w(x)u'(x)$ we can compute F_k , $k = 1, 2, \dots$ using the formula

$$F_k = W_0 U_k + \frac{1}{k} \sum_{j=0}^{k-1} j U_j W_{k-j},$$

see also [17].

Here we are interesting in approximating $\cos(\varphi_x + 1)$ and thus note that the functions $s(x) = \sin(u(x))$ and $c(x) = \cos(u(x))$ satisfy $s'(x) = c(x)u'(x)$ and $c'(x) = -s(x)u'(x)$ simultaneously. Thus, we use both relationships and the formula above to obtain $\cos(\varphi_x + 1)$. Precisely, first we compute

$$(\varphi_x)_k = \begin{cases} \frac{k+1}{h} \varphi_k & \text{if } k = 0 \dots 2m, \\ 0 & \text{if } k = 2m + 1, \end{cases}$$

followed by

$$u_k = \begin{cases} (\varphi_x)_k + 1 & \text{if } k = 0, \\ (\varphi_x)_k & \text{if } k = 1, \dots, 2m + 1. \end{cases}$$

We then set $c_0 = \cos(u_0)$ and $s_1 = \sin(u_0)$ and update the remaining coefficients using the recursion

$$\begin{aligned} s_k &= c_0 u_k + \mathbf{d\dot{d}ot}(c, u, k), \\ c_k &= -s_0 u_k - \mathbf{d\dot{d}ot}(s, u, k), \end{aligned}$$

where $u = [u_0, u_1, \dots, u_{2m+1}]^T$, $c = [c_0, c_1, \dots, c_{2m+1}]^T$, $s = [s_0, s_1, \dots, s_{2m+1}]^T$ and $\mathbf{d\dot{d}ot}$ is the function is given by

$$\mathbf{d\dot{d}ot}(A, B, k) = \frac{1}{k} \sum_{j=0}^{k-1} j A_j B_{k-j}.$$

The c_k are the Taylor coefficients of the polynomial approximating $\cos(\varphi_x + 1)$.

In Table 1 we display the L_1 , L_2 and L_∞ norm errors for $H(\varphi_x) = -\cos(\varphi_x + 1)$ using $x_l = 0$, $x_r = 2\pi$ using $n_x = 20, 40, 80$ and 160 gridpoints. As can be seen from the estimated rates of convergence the procedure is as accurate as the Hermite interpolation (h^{2m+2}). To the left in Figure 1 we plot the Taylor series approximation which can be seen to be accurate.

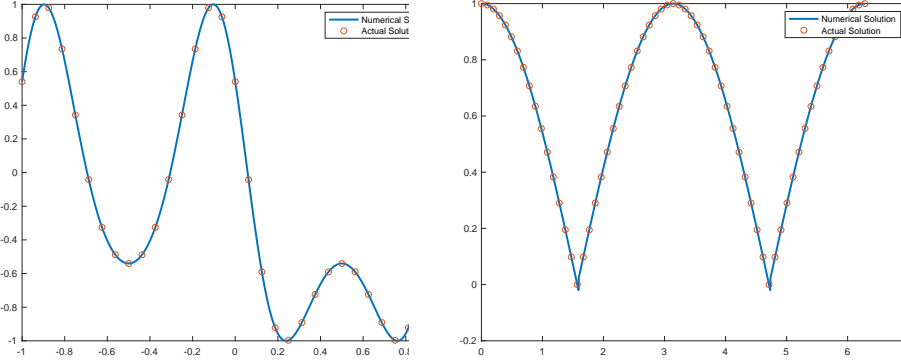


Fig. 1 On the left we plot the numerical approximation to $H(\varphi_x) = -\cos(\varphi_x + 1)$ as a solid line and sample the actual function as circles. On the right we plot the numerical approximation to $H(\varphi_x) = -|\varphi_x|$ as a solid line and sample the actual function as circles. In both cases we used $m = 3$ derivatives.

Table 1 Errors in approximating $H(\varphi_x) = -\cos(\varphi_x + 1)$ using Taylor series approximation recursions in the L_1 , L_2 and L_∞ norms at time are displayed along with estimated rates of convergence. Note that we obtain the expected rate of $2m + 2$ where m is the number of derivatives used in approximation.

n	L_1 error	Convergence	L_2 error	Convergence	L_∞ error	Convergence
$m = 2$						
20	1.18e-05	-	1.95e-05	-	5.05e-05	-
40	1.75e-07	6.08	3.07e-07	5.99	9.89e-07	5.68
80	2.74e-09	5.99	4.86e-09	5.98	1.61e-08	5.94
160	4.44e-11	5.95	7.94e-11	5.94	2.71e-10	5.90
$m = 3$						
20	1.42e-07	-	2.64e-07	-	7.65e-07	-
40	5.69e-10	7.96	1.04e-09	7.99	3.37e-09	7.83
80	2.19e-12	8.02	4.06e-12	8.00	1.32e-11	8.00
160	8.93e-15	7.94	1.59e-14	8.00	5.20e-14	7.99

In the case of a Hamiltonian with an absolute value function the above procedure cannot be used. We now describe how to handle such cases using the Eikonal equation

$$\varphi_t + |\varphi_x| = 0,$$

as an example. Here, we need the expansion of $|\varphi_x|$. If φ_x is not sign definite, then we can not use the method above to obtain a Taylor series expansion and instead we proceed by computing

$$(\varphi_x)_k = \begin{cases} \frac{k+1}{h} \varphi_k & \text{if } k = 0 \dots 2m, \\ 0 & \text{if } k = 2m + 1. \end{cases}$$

At the cell center the value of the function is given by the leading coefficient. That is, $\varphi_x(x_i) = \varphi_0$. Therefore, as an approximation we take

$$|(\varphi_x)_k| = \begin{cases} (\varphi_x)_k & \text{if } \varphi_0 \geq 0, \\ -(\varphi_x)_k & \text{if } \varphi_0 < 0. \end{cases}$$

In Table 1 we display the L_1 , L_2 and L_∞ norm errors for $H(\varphi_x) = |\varphi_x|$ using $x_l = 0$, $x_r = 2\pi$ with $n_x = 20, 40, 80$ and 160 gridpoints. We show the estimated rates of convergence for each norm. Of course here we cannot expect the full order of convergence as the nonlinearity is not smooth. To the right in Figure 1 we plot the Taylor series approximation, which can be seen to be an accurate approximation to the true Hamiltonian.

Table 2 Errors in approximating $H(\varphi_x) = |\varphi_x|$ using Taylor series in the L_1 , L_2 and L_∞ norms at time are displayed along with estimated rates of convergence. Note that the function we are trying to interpolate is nonlinear, thus we do not obtain the expected rate of $2m + 2$ where m is the number of derivatives used in approximation.

n	L_1 error	Convergence	L_2 error	Convergence	L_∞ error	Convergence
$m = 2$						
20	6.15e-02	-	1.20e-01	-	3.13e-01	-
40	1.54e-02	2.00	4.26e-02	1.50	1.57e-01	1.00
80	3.85e-03	2.00	1.51e-02	1.50	7.85e-02	1.00
160	9.64e-04	2.00	5.33e-03	1.50	3.93e-02	1.00
$m = 3$						
20	6.15e-02	-	1.20e-01	-	3.13e-01	-
40	1.54e-02	2.00	4.26e-02	1.50	1.57e-01	1.00
80	3.85e-03	2.00	1.51e-02	1.50	7.85e-02	1.00
160	9.64e-04	2.00	5.33e-03	1.50	3.93e-02	1.00

2.1.4 Second Half-step and Boundary Conditions

To complete a full time step we repeat this procedure, starting with the initial data obtained from evolving (10) a half-step $\Delta t/2$ on the dual grid. At the interior nodes x_i , $i = 1, \dots, n_x - 1$ the procedure is the same as above, but at the boundary nodes we must fill in ghost polynomials at $x_{i-\frac{1}{2}}$ and $x_{n_x+\frac{1}{2}}$, for example by using the properties of the PDE or as in the case of periodic boundary conditions considered here by simply copying data from the opposite boundary.

2.2 Hermite Method in Two-Dimensions

The method in higher dimensions is a direct tensor product extension of the one dimensional procedure. We now describe the method for the Hamilton-Jacobi equation in two-dimensions, with periodic boundary conditions

$$u_t = \begin{cases} \varphi_t + H(\varphi_x, \varphi_y) = 0, \\ \varphi(x, y, 0) = \varphi^0(x, y), \end{cases} \quad (11)$$

and on the rectangular domain $D = [x_L, x_R] \times [y_B, y_T]$.

2.2.1 Initialization

We discretize the grid as follows,

$$(x_i, y_j) = (x_L + ih_x, y_B + jh_y), \quad (12)$$

where $h_x = (x_R - x_L)/N_x$ and $h_y = (y_T - y_B)/N_y$ where $i = 0, \dots, n_x$, $j = 0, \dots, n_y$ for the primal grid and $i = 1/2, \dots, n_x - 1/2$, $j = 1/2, \dots, n_y - 1/2$ for the dual grid.

The first step initialize the degrees of freedom by setting them to be the scaled derivatives at each point on the primal grid

$$c_{l_x, l_y} = \frac{h_x^{l_x}}{l_x!} \frac{h_y^{l_y}}{l_y!} \left. \frac{d^{l_x} d^{l_y} u(x, 0)}{dx^{l_x} dy^{l_y}} \right|_{(x=x_i, y=y_j)}.$$

Note that $c_{l_x, l_y} = c_{l_x, l_y, i, j}$, but we suppress the spatial indices for notational convenience. We interpolate onto the dual grid to obtain the tensor-product Taylor polynomials

$$v_{i+\frac{1}{2}, j+\frac{1}{2}}(x, y, 0) = \sum_{l_x=0}^{2m+1} \sum_{l_y=0}^{2m+1} d_{l_x, l_y} \left(\frac{x - x_{i+\frac{1}{2}}}{h_x} \right)^{l_x} \left(\frac{y - y_{j+\frac{1}{2}}}{h_y} \right)^{l_y}, \quad (13)$$

where the polynomial interpolates the function values and the partial derivatives at the four corners of the cell. Algorithmically, forming of the interpolant is done by repeated one-dimensional interpolation. For example, we may interpolate in the y direction, for the function and all the x derivatives at grid points (x_i, y_j) and (x_i, y_{j+1}) to obtain one interpolant centered at $(x_i, y_{j+1/2})$ and from (x_{i+1}, y_j) and (x_{i+1}, y_{j+1}) to obtain another interpolant centered at $(x_{i+1}, y_{j+1/2})$. These two polynomials of degree m in x and degree $2m + 1$ in y are then interpolated in the x direction using one-dimensional interpolation. The final result is a polynomial on the form (13).

2.2.2 Evolution

Similar to the one-dimensional case, we treat the coefficients in the Hermite expansions as functions of time. That is, we expand

$$v_{i+1/2, j+1/2}(x, y, t) = \sum_{l_x=0}^{2m+1} \sum_{l_y=0}^{2m+1} d_{l_x, l_y}(t) \left(\frac{x - x_{i+1/2}}{h_x} \right)^{l_x} \left(\frac{y - y_{j+1/2}}{h_y} \right)^{l_y}. \quad (14)$$

For our PDE $\varphi_t = -H(\varphi_x, \varphi_y)$ we substitute (14):

$$\begin{aligned} \frac{\partial v_{i+1/2}(x, y, t)}{\partial t} &= \sum_{l_x=0}^{2m+1} \sum_{l_y=0}^{2m+1} d'_{l_x, l_y}(t) \left(\frac{x - x_{i+1/2}}{h_x} \right)^{l_x} \left(\frac{y - y_{j+1/2}}{h_y} \right)^{l_y} \\ &= -H(\varphi_x, \varphi_y). \end{aligned} \quad (15)$$

We differentiate in (15) k times in the x -coordinate and l times in the y -coordinate and evaluate at $(x, y) = (x_{i+1/2}, y_{j+1/2})$ to obtain

$$\frac{k!}{h_x^k} \frac{l!}{h_y^l} d'_{k, l}(t) = - \left. \frac{\partial^k}{\partial x^k} \frac{\partial^l}{\partial y^l} H(v_x, v_y) \right|_{(x, y) = (x_{i+1/2}, y_{j+1/2})}. \quad (16)$$

Similar to the one-dimensional case, the differentiation of a non-linear H can spawn new terms by the product rule. We avoid this by approximating the Hamiltonian by a Taylor polynomial of degree $(2m+1) \times (2m+1)$

$$H(v_x, v_y) \approx \sum_{l_x=0}^{2m+1} \sum_{l_y=0}^{2m+1} b_{l_x, l_y}(t) \left(\frac{x - x_{i+1/2}}{h_x} \right)^{l_x} \left(\frac{y - y_{j+1/2}}{h_y} \right)^{l_y}. \quad (17)$$

From (15) and (17) we obtain the local system of ODEs

$$d'_{l_x, l_y}(t) = b_{l_x, l_y}(t), \quad l_x = 0, \dots, 2m+1, \quad l_y = 0, \dots, 2m+1. \quad (18)$$

We can evolve the solution of this system using, e.g., a Runge-Kutta method.

2.2.3 Boundary Conditions for the Second Half-step

To complete a full time step we repeat this procedure, starting with the initial data obtained from evolving (18) a half-step on the dual grid. At the interior nodes (x_i, y_j) , $i = 1, \dots, n_x - 1$, $j = 1, \dots, n_y - 1$ the procedure is the same as above, but at the boundary nodes we must fill in ghost polynomials. In our case we use the periodic boundary conditions to fill in the ghost polynomials.

3 Adopting the Person-Peraire, Klockner-Warburton-Hesthaven Sensor to Hermite Methods

3.1 Estimating Smoothness

The smoothness detector used to modify our Hermite method is an adaptation of the sensor in [19]. The sensor uses orthogonal polynomials, $\{\phi_n\}_{n=0}^{N_p-1}$, on each cell to estimate the smoothness of the solution, where N_p is the degree of the expansion basis. The method developed here also utilizes the improvements to the Person-Peraire sensor proposed by Klockner, Warburton and Hesthaven in [15].

On each element D_k , the Person-Peraire sensor computes a smoothness indicator

$$S_k = \frac{(q_N, \phi_{N_p-1})_{L^2(D_k)}^2}{\|q_N\|_{L^2(D_k)}^2}, \quad (19)$$

where N is the degree of the interpolating polynomials. For the one-dimensional smoothness estimator we use the Legendre basis and in the two dimensional case we form the tensor-products of the one-dimensional Legendre polynomials; therefore, we take $N = 2m + 1$ and $N_p = 2m + 1$. We assume that, for the modal coefficients $\{\hat{q}_n\}_{n=0}^{N_p-1}$ of a function $q_N \in L^2$ spanned by $\{\phi_n\}_{n=0}^{N_p-1}$, the modal decay is representable as

$$|\hat{q}_n| \sim cn^{-s}, \quad (20)$$

Taking the logarithm of (20) we have

$$\log |\hat{q}_n| \approx \log(c) - s \log(n), \quad (21)$$

we may find the c and s via least squares fitting, we minimize

$$\sum_{n=1}^{N_p-1} |\log |\hat{q}_n| - (\log(c) - s \log(n))|^2, \quad (22)$$

note here that the sum begins at $n = 1$, thus the constant coefficient data is not taken into account when estimating smoothness.

The removal of the constant-mode information from the estimation process can cause problems. The sensor can be thrown off by white noise if we have a constant function. The sensor can not determine that the noise is small in comparison to the function. A fix to this problem, introduced in [15], is a technique called *baseline modal decay*. Heuristically, the idea is to re-add the sense of scale by distributing the energy according to a perfect modal decay

$$|\hat{b}_n| \sim C \frac{1}{n^N}, \quad (23)$$

for N the polynomial degree of the method, the normalizing factor C ensures that

$$\sum_{n=1}^{N_p-1} |\hat{b}_n|^2 = 1.$$

We input the coefficients

$$|\tilde{q}_n|^2 := |\hat{q}_n|^2 + \|q_N\|_{L^2(D_k)}^2 |b_k|^2 \quad \text{for } n \in \{1, \dots, N_p - 1\}, \quad (24)$$

into skyline pessimization (described below), instead of the raw coefficients $|\hat{q}_n|$.

There are certain situations where the estimator can be fooled. For example, when interpolating the function $x\Theta(x)$, where $\Theta(x)$ is the Heavyside function, [15] shows that there is an odd - even effect for which odd modes greater than three are numerically zero. A correction of this problem was given by introducing a technique named *skyline pessimization*. The idea is as follows: if you have a mode n with a small coefficient $|\hat{q}_n|$ such that there exists another coefficient with $m > n$ and $|\hat{q}_m| \gg |\hat{q}_n|$, then the coefficient $|\hat{q}_n|$ is most likely spurious and should not be taken into account when estimating s . Therefore, the idea is to generate a new set of modal coefficients by

$$\bar{q}_n := \max_{i \in \{\min(n, N_p - 2), \dots, N_p - 1\}} |\hat{q}_i| \quad \text{for } n \in \{1, 2, \dots, N_p - 1\}. \quad (25)$$

This forces each modal coefficient to be raised up to the largest higher-numbered modal coefficient, eliminating non-monotone decay.

3.2 Computing the Viscosity from the Smoothness Sensor

3.2.1 Implementation in One-Dimension

At each time step, t_k , we approximate the smoothness of the function inside each cell. In order to determine the modal coefficients, $\{\hat{q}_n\}$, we take $2m + 1$ Legendre-Gauss-Lobatto nodes (see Figure 2) z_i and map the nodes in $[-1, 0]$ to $[x_k, x_{k+1/2}]$ and the nodes in $[0, 1]$ to $[x_{k+1/2}, x_{k+1}]$, then we evaluate the Hermite interpolants $p_k(x)$ in $[x_k, x_{k+1/2}]$ and $p_{k+1}(x)$ in $[x_{k+1/2}, x_{k+1}]$ on the nodes to obtain the function values required for projection. Once the projection is completed, we compute $\{\hat{q}_n\}$ and approximate s using (21).

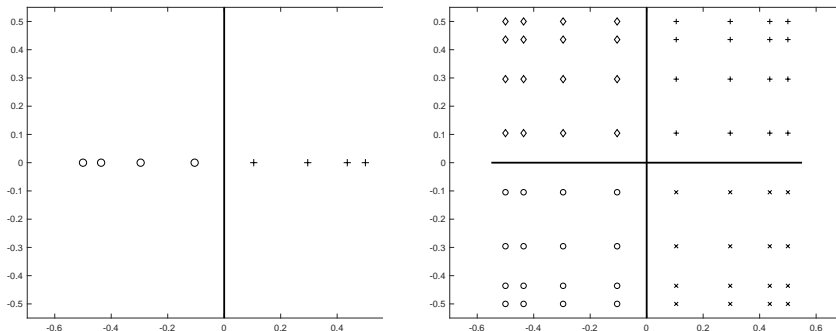


Fig. 2 Left LGL nodes in one-dimension; Right LGL nodes in two-dimensions.

If the solution is no longer C^1 , then we introduce numerical viscosity by taking $1 - \kappa_w(s)$ where s is the smoothness estimate and $\kappa_w(s)$ is given by [19] as

$$\kappa_w(s) = \nu_0 \begin{cases} 0 & s_w < s_0 - w, \\ \frac{1}{2} \left(1 + \sin \frac{\pi(s_w - s_0)}{2w} \right) & s_0 - w \leq s_w \leq s_0 + w, \\ 1 & s_0 + w < s_w, \end{cases} \quad (26)$$

where we choose $s_0 = 2$ and $s_w = 3$. These choices activates the viscosity as soon as the solution fails to be C^1 , $s = 3$, and gives maximum viscosity, ν_0 , when the solution is C^0 .

We set the maximum viscosity, ν_0 , to be

$$\nu_0 = \lambda \frac{h}{N}, \quad (27)$$

where λ is the maximum local characteristic velocity. We estimate λ by taking the derivative of the Hamiltonian with respect to φ_x at each cell center and taking the maximum of the absolute value:

$$\lambda = \max_i |H_{v_x}(v_x(x_{i+\frac{1}{2}}))|. \quad (28)$$

Note that this value is directly accessible, as v_x is part of the degrees of freedom.

Before modifying the PDE we average the viscosity in the spatial domain by setting

$$\bar{\kappa}_i = \frac{1}{4}(\kappa_{i-1} + 2\kappa_i + \kappa_{i+1}).$$

We introduce the numerical viscosity at each timestep when evolving our PDE after interpolation. That is, after the interpolation step we modify the PDE by adding $\bar{v}_i u_{xx}$ making the equation

$$v_t + H(v_x) = \bar{\kappa}_i v_{xx}, \quad (29)$$

on the i th cell.

3.2.2 Implementation in Two-Dimensions

As our orthogonal basis we choose the tensor-product of Legendre polynomials. To check the smoothness of a cell we use the nearest interpolants on the other grid located on the four corners of the cell. That is, if the smoothness information for the cell centered at $(x_{k+1/2}, y_{l+1/2})$ then we use the Hermite interpolants at (x_k, y_l) , (x_{k+1}, y_l) , (x_k, y_{l+1}) , and (x_{k+1}, y_{l+1}) . As in one dimension, we partition the cell into four regions and evaluate the function on each region using the interpolant that corresponds to it. For example, for the lower left region we use the information from the Hermite interpolant centered at (x_k, y_l) .

We analyze the decay of coefficients by grouping them by the total degree i.e., the degree of Legendre polynomial in x plus the degree of the Legendre polynomial in y . The tensor-product Legendre polynomial is of the form

$$p = \sum_{k=0}^{2m+1} \sum_{l=0}^{2m+1} C_{k,l} \phi_k \phi_l, \quad (30)$$

where ϕ_k and ϕ_l are the Legendre polynomials in one-dimension.

There are several ways to order the polynomials in each degree; however, some orderings will fool the sensor. We take the maximum coefficient in absolute value for each total degree and use that as our input to the sensor for that degree. That is, we take $c_i = \max |C_{k,l}|$, where $k + l = i$. Once we obtain this ordering we apply *baseline modal decay* and *skyline pessimization* in the same way as the one-dimensional case.

We set the maximum viscosity, ν_0 , to be

$$\nu_0 = \lambda \frac{h}{N}, \quad (31)$$

where N is the degree of the Hermite interpolating polynomial in one coordinate direction and $h = \max\{h_x, h_y\}$. For estimating λ we adapt the Lax-Friedrichs flux given in [8,18] by taking the partial derivatives of the Hamiltonian with respect to φ_x and φ_y evaluating them at the cell centers and taking the maximum of the absolute value:

$$\lambda = \max_{i,j} \{ |H_{v_x}(v_x(x_{i+\frac{1}{2}}, y_{j+\frac{1}{2}}), v_y(x_{i+\frac{1}{2}}, y_{j+\frac{1}{2}}))|, |H_{v_y}(v_x(x_{i+\frac{1}{2}}, y_{j+\frac{1}{2}}), v_y(x_{i+\frac{1}{2}}, y_{j+\frac{1}{2}}))| \}. \quad (32)$$

Before modifying the PDE we average the viscosity in the spatial domain by setting

$$\bar{\kappa}_{k,l} = \frac{1}{16} (\kappa_{k-1,l-1} + \kappa_{k+1,l-1} + \kappa_{k-1,l+1} + \kappa_{k+1,l+1} + 2(\kappa_{k,l-1} + \kappa_{k-1,l} + \kappa_{k+1,l} + \kappa_{k,l+1}) + 4\kappa_{k,l}).$$

We introduce the numerical viscosity at each timestep when evolving our PDE after interpolation. That is, after the interpolation step we modify the PDE making the equation

$$v_t + H(v_x, v_y) = \bar{\kappa}_{k,l}(v_{xx} + v_{yy}). \quad (33)$$

In Figure 3 we test the smoothness sensor on two discontinuous functions, a radially symmetric step function and an oblique step function. In both cases the sensor correctly determines the level of smoothness of the underlying function.

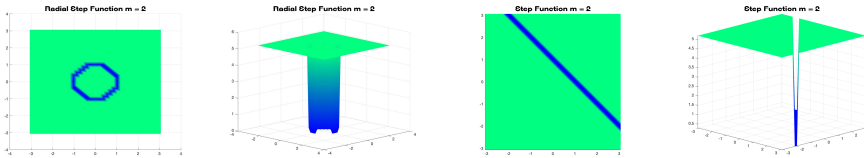


Fig. 3 Top: different views of the smoothness sensor when applied to a radial stepfunction $f(x) = 1$ if $r^2 \leq 1$ and zero otherwise. In the smooth region the smoothness is estimated to be 5 and near the the discontinuity it is estimated to be approximately 1/2. Bottom: different views of the smoothness sensor for a stepfunction with $f(x) = 1$ if $x+y \leq 1$ and zero otherwise. The results are similar to the radial case.

4 Numerical Examples

For each of the following examples we expect the convergence rate to be $2m + 1$ when the solution is smooth, where m is number of derivatives used in the interpolation process. When the solution fails to remain smooth we do not expect to see the optimal convergence rates, instead we seek sharp resolution of kinks. For each example we give convergence rates at a time when the solution is still smooth. For the timestepping we use the classical Runge-Kutta method of order 4 (RK4). To this end we chose the timestep small enough so that the temporal error is dominated by the spatial error.

4.1 Examples in One Dimension

Table 3 Errors in Example 1 in the L_1 , L_2 and L_∞ norms at time $T = 0.5$ are displayed along with estimated rates of convergence.

n	L_1 error	Conv. Rate	L_2 error	Conv. Rate	L_∞ error	Conv. Rate
$m = 2$						
20	6.86e-06	-	7.30e-06	-	1.54e-05	-
40	2.27e-07	4.92	2.22e-07	5.04	5.17e-07	4.90
80	7.28e-09	4.96	6.99e-09	4.99	1.57e-08	5.04
160	2.41e-10	4.92	2.30e-10	4.93	4.98e-10	4.98
$m = 3$						
20	4.44e-07	-	5.68e-07	-	1.26e-06	-
40	2.85e-09	7.28	3.43e-09	7.37	8.49e-09	7.21
80	2.04e-11	7.13	2.55e-11	7.07	6.23e-11	7.09
160	1.83e-13	6.80	1.87e-13	7.10	4.56e-13	7.10

4.1.1 Example 1

In this example we solve the one-dimensional Burgers' equation

$$\varphi_t + \frac{1}{2}\varphi_x^2 = 0,$$

with initial condition $\varphi(x, 0) = \sin(x)$ and with periodic boundary conditions $\varphi(0, t) = \varphi(2\pi, t)$. The solution is smooth until time $T = 1.0$, at this time a shock will form in φ_x . Our grid is determined by $x_l = 0$, $x_r = 2\pi$ and the number of grid points, n_x . For this example we start with $n_x = 20$ and refine the grid by a factor of two until $n_x = 160$ in order to demonstrate convergence to the viscosity solution. Before the solution develops a kink we demonstrate that our method achieves $2m + 1$ order accuracy at time $T = 0.5$ as evidenced by the errors measured in the L_1, L_2 and L_∞ -norm along with the estimated rates of convergence reported in Table 3. We also demonstrate that we converge to the viscosity solution at time $T = 1.5$ in Figure 4 along with the errors reported in Table 4.

The convergence rates displayed in the tables show us that we are converging to the viscosity solution as the grid is being refined. We observe in Figure 4 that the method is able to capture the kink formed at $\frac{\pi}{2}$. In Figure 5 we see that as we refine the grid the error is localized where the kink is formed.

4.1.2 Example 2

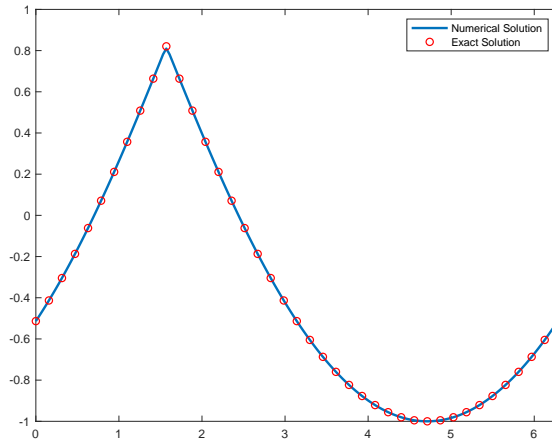
In this example we solve the one-dimensional Eikonal equation

$$\varphi_t + |\varphi_x| = 0,$$

with initial condition $\varphi(x, 0) = \sin(x)$ and with periodic boundary conditions. The viscosity solution to this equation has a shock forming in φ_x at $x = \pi/2$ and a rarefaction wave at $x = 3\pi/2$. The solution is nonsmooth for all $T > 0$ so we do

Table 4 Errors in Example 1 in the L_1 , L_2 and L_∞ norms at time $T = 1.5$ are displayed along with estimated rates of convergence. Note that these errors occur after a kink has formed.

n	L_1 error	Conv. Rate	L_2 error	Conv. Rate	L_∞ error	Conv. Rate
$m = 2$						
20	1.16e-02	-	1.71e-02	-	4.00e-02	-
40	2.73e-03	2.09	5.86e-03	1.54	1.97e-02	1.02
80	6.81e-04	2.00	2.08e-03	1.50	9.85e-03	1.00
160	1.70e-04	2.00	7.28e-04	1.51	4.87e-03	1.01
$m = 3$						
20	6.87e-03	-	1.46e-02	-	3.67e-02	-
40	1.66e-03	2.05	4.94e-03	1.57	1.75e-02	1.07
80	4.12e-04	2.01	1.75e-03	1.50	8.75e-03	1.00
160	1.02e-04	2.01	6.18e-04	1.50	4.38e-03	1.00

**Fig. 4** Example 1 at time $t = 1.5$ well after the kink has developed. This computation was done with $m = 3$ and $N = 80$ cells. The solid line is the numerical solution and the dots are the exact solution.

not expect order $2m + 1$ convergence. To analyze the convergence we use the same grids as in Example 1. We report the L_1 , L_2 and L_∞ errors and their estimated rates of convergence in Table 5. In Figure 6 we plot the numerical solution to demonstrate convergence to the viscosity solution.

The convergence rates displayed in the tables show us that we are converging to the viscosity solution as the grid is being refined. We observe in Figure 6 that the method is able to capture the kink formed at $\frac{\pi}{2}$ and the rarefaction wave at $\frac{3\pi}{2}$. In Figure 7 we see that as we refine the grid the error is localized where the kink is formed. We briefly note that the discontinuity in the Hamiltonian, H , causes the piece-wise interpolant to lose smoothness in between cells where the sign of φ_x changes. We plan to see if we can rectify this by using a flux-conservative formulation of this method.

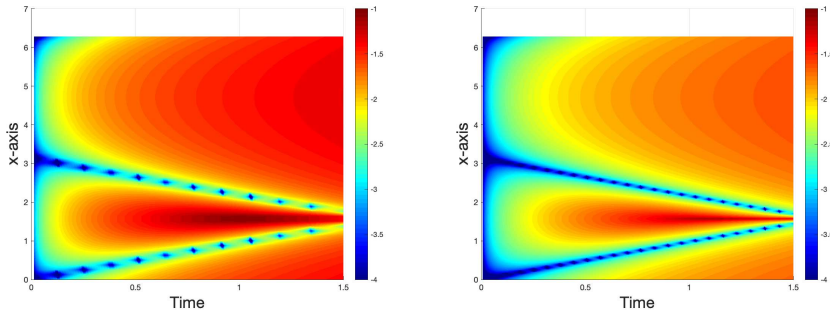


Fig. 5 Here we display the evolution of the errors with a refinement. On the left we display the evolution of errors with 50 cells and on the right we display the evolution of errors with 100 cells.

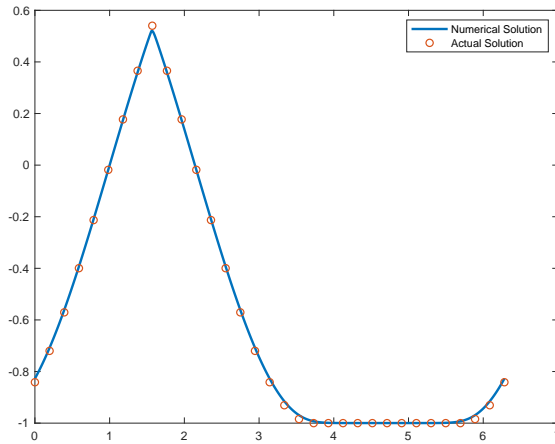


Fig. 6 Example 2 at time $t = 1.0$ with $m = 3$ and $N = 80$ cells the solid line is the numerical solution and the dots are exact solution.

4.1.3 Example 3

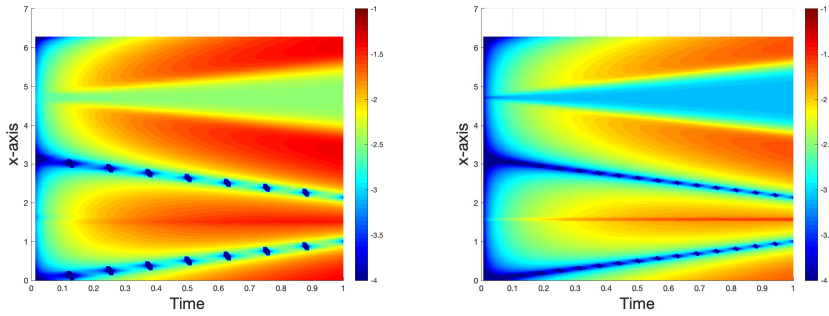
In this example we solve a one-dimensional equation with a nonconvex Hamiltonian

$$\varphi_t - \cos(\varphi_x + 1) = 0,$$

with initial condition $\varphi(x, 0) = -\cos(\pi x)$ and periodic boundary conditions $\varphi(-1, t) = \varphi(1, t)$. This example shows that our scheme has high-order accuracy even when the Hamiltonian is not convex. Our grid is determined by $x_l = -1$, $x_r = 1$ and the number of grid points, n_x . For this example we start with $n_x = 20$ and refine the grid until $n_x = 160$ in order to demonstrate convergence to the viscosity solution. Before the solution develops a kink we demonstrate our method achieves $2m + 1$ order accuracy at time $T = \frac{0.5}{\pi^2}$ by giving the L_1 , L_2 and L_∞ -norm along with the estimated rates of convergence in Table 6. We also demonstrate that we converge to the viscosity solution at time $T = \frac{1.5}{\pi^2}$ in Figure 8.

Table 5 Errors in Example 2 in the L_1 , L_2 and L_∞ norms at time $T = 1.0$ are displayed along with estimated rates of convergence.

n	L_1 error	Conv. Rate	L_2 error	Conv. Rate	L_∞ error	Conv. Rate
$m = 2$						
20	4.84e-01	-	2.20e-01	-	1.94e-01	-
40	2.35e-01	1.04	1.13e-01	0.96	1.09e-01	0.83
80	1.14e-01	1.04	5.77e-02	0.97	5.79e-02	0.91
160	5.60e-02	1.03	2.93e-02	0.98	2.98e-02	0.96
$m = 3$						
20	3.40e-01	-	1.58e-01	-	1.39e-01	-
40	1.65e-01	1.04	8.11e-02	0.97	7.61e-02	0.87
80	8.05e-02	1.04	4.13e-02	0.97	3.96e-02	0.94
160	3.97e-02	1.02	2.10e-02	0.98	2.03e-02	0.97

**Fig. 7** Here we display the evolution of the errors with a refinement. On the left display the evolution of errors with 50 cells and on the right we display the evolution of errors with 100 cells.**Table 6** Errors in Example 3 in the L_1 , L_2 and L_∞ norms at time $T = 0.5/\pi^2$ are displayed along with estimated rates of convergence.

$m = 2$						
n	L_1 error	Conv. Rate	L_2 error	Conv. Rate	L_∞ error	Conv. Rate
20	1.72e-05	-	3.49e-05	-	1.59e-04	-
40	4.67e-07	5.20	1.05e-06	5.06	6.47e-06	4.62
80	1.48e-08	4.98	2.63e-08	5.32	1.68e-07	5.27
160	6.56e-10	4.50	8.62e-10	4.93	3.79e-09	5.47
$m = 3$						
20	4.96e-06	-	1.18e-05	-	5.77e-05	-
40	4.00e-08	6.95	1.31e-07	6.50	8.79e-07	6.04
80	2.23e-10	7.48	7.28e-10	7.49	4.75e-09	7.53
160	1.94e-12	6.84	4.30e-12	7.40	3.17e-11	7.23

The convergence rates displayed in the tables show us that we are converging to the viscosity solution as the grid is being refined. We observe in Figure 8 that the method is able to capture the kinks formed in this example.

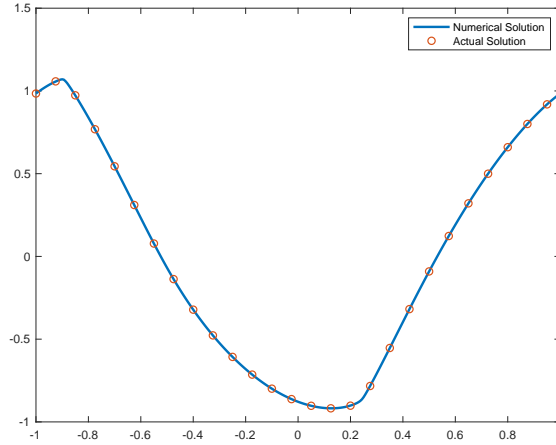


Fig. 8 Example 3 at time $t = 1.5/\pi^2$ with $m = 3$ using $N = 80$ cells. The solid line is the numerical solution and the dots are the exact solution

Table 7 Errors in Example 4 in the L_1 , L_2 and L_∞ norms at time $T = 0.1$ are displayed along with estimated rates of convergence.

$m = 2$						
n	L_1 error	Conv. Rate	L_2 error	Conv. Rate	L_∞ error	Conv. Rate
10	4.77e-03	-	3.78e-04	-	8.76e-04	-
20	1.77e-04	4.75	1.43e-05	4.72	3.91e-05	4.49
40	5.72e-06	4.95	5.77e-07	4.63	1.33e-06	4.88
80	1.81e-07	4.98	2.46e-08	4.55	4.23e-08	4.98
$m = 3$						
10	1.28e-04	-	1.41e-05	-	4.29e-05	-
20	9.70e-07	7.05	4.90e-08	8.17	3.62e-07	6.89
40	7.45e-09	7.02	2.67e-10	7.52	2.50e-09	7.18
80	5.66e-11	7.04	2.15e-12	6.96	1.88e-11	7.06

4.2 Examples in Two Dimensions

4.2.1 Example 4

In this example we solve the two-dimensional Burgers' equation

$$\varphi_t + \frac{1}{2}(\varphi_x + \varphi_y)^2 = 0,$$

with initial condition $\varphi(x, y, 0) = -\cos(x + y)$ and periodic boundary conditions on $[0, 2\pi]^2$. This equation can be reduced to a one-dimensional equation via the change of variables $z = \frac{x+y}{2}$. That is,

$$\begin{aligned} \frac{\partial u}{\partial z} &= \frac{\partial u}{\partial z} \frac{\partial z}{\partial x} + \frac{\partial u}{\partial z} \frac{\partial z}{\partial y} \\ &= \frac{1}{2} \frac{\partial u}{\partial z} + \frac{1}{2} \frac{\partial u}{\partial z} \\ &= \frac{\partial u}{\partial z}. \end{aligned}$$

Thus, our equation becomes

$$\varphi_t + \frac{1}{2}\varphi_z^2 = 0,$$

with initial condition $\varphi(z, 0) = -\cos(2z)$ and periodic boundary conditions on $[0, 2\pi]$.

We use the grid with $x_L, y_B = 0$ and $x_R, y_T = 2\pi$ with $n_x, n_y = 10$ cells and refine the grid by a factor of two until we have $n_x, n_y = 80$ cells in order to demonstrate convergence to the viscosity solution. Before the solution develops a kink we demonstrate our method achieves $2m + 1$ order accuracy at time $T = 0.1$ by giving the L_1, L_2 and L_∞ -norm along with the estimated rates of convergence in Table 7. We also demonstrate the development of singular features in Figure 9.

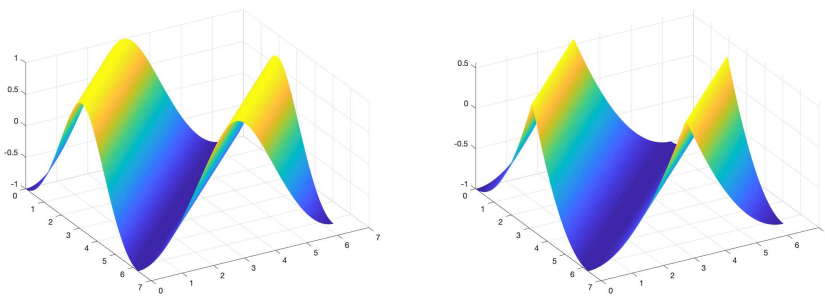


Fig. 9 Example 4 on the left is the numerical solution at time $t = 0.1$ approximated using $m = 3$ derivatives on $N = 40$ cells on the right is the numerical solution at time $t = 0.5$ using the same number of derivatives and cells.

We see from the table that we obtain the full order of the method while the solution is smooth. The figure shows us how the method is able to capture the singular features of the solution.

4.2.2 Example 5

In this example we solve a two-dimensional nonlinear equation

$$\varphi_t + \varphi_x \varphi_y = 0,$$

with initial condition $\varphi(x, y, 0) = \sin(x) + \cos(y)$ and periodic boundary conditions on the domain $[-\pi, \pi]^2$.

This is a genuinely nonlinear problem with a nonconvex Hamiltonian. The viscosity solution is smooth at time $T = 0.5$; we demonstrate $2m + 1$ convergence at this time. By $T = 1.5$ the viscosity solution develops singular features. We use the grid with $x_L, y_B = -\pi$ and $x_R, y_T = \pi$ with $n_x, n_y = 10$ cells and refine the grid by a factor of two until we have $n_x, n_y = 80$ cells in order to demonstrate convergence to the viscosity solution. Before the solution develops singular features

we demonstrate our method achieves $2m + 1$ order accuracy at time $T = 0.5$ by giving the L_1 , L_2 and L_∞ -norm along with the estimated rates of convergence in Table 8. We also demonstrate the singular features that the solution develops in Figure 10

Table 8 Errors in Example 5 in the L_1 , L_2 and L_∞ norms at time $T = 0.5$ are displayed along with estimated rates of convergence.

n	L_1 error	Convergence	L_2 error	Convergence	L_∞ error	Convergence
$m = 2$						
10	3.50e-04	-	6.78e-05	-	2.18e-05	-
20	1.08e-05	5.02	2.11e-06	5.00	6.89e-07	4.98
40	3.35e-07	5.01	6.58e-08	5.00	2.14e-08	5.01
80	1.04e-08	5.01	2.05e-09	5.00	6.64e-10	5.01
$m = 3$						
10	2.62e-07	-	5.15e-08	-	1.76e-08	-
20	1.95e-09	7.07	3.86e-10	7.06	1.33e-10	7.05
40	1.48e-11	7.04	2.96e-12	7.03	1.00e-12	7.05
80	1.17e-13	6.98	2.52e-14	6.87	1.51e-14	6.05

This example is truly a two-dimensional nonlinear problem and we still see that we obtain the full order of the method while the solution is smooth and our method is able to capture the singular features of the solution.

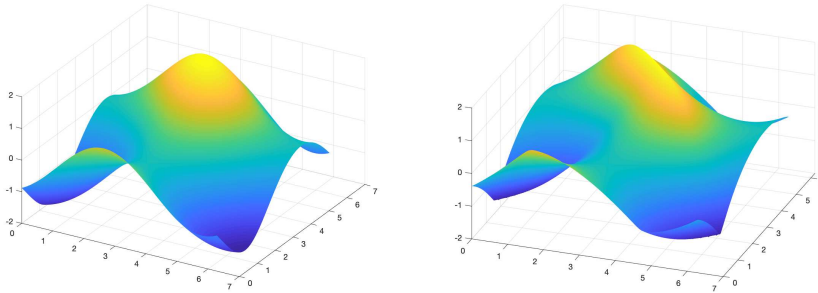


Fig. 10 Example 5 on the left is the numerical solution at time $t = 0.5$ approximated using $m = 3$ derivatives on $N = 40$ cells on the right is the numerical solution at time $t = 1.5$ using the same number of derivatives and cells.

5 Conclusions and Future Work

Through the coupling of Hermite methods and a discontinuity sensor, our method attains $2m + 1$ order of convergence in smooth regions while converging to the viscosity solution when kinks are present. While we were able to achieve the goals of: 1) high order accuracy in smooth regions and 2) sharp resolution of kinks, we

believe that there are several ways this method can be improved upon. The Eikonal equation gave us inspiration to develop a flux-conservative Hermite method for HJ equations in order to keep continuity in the derivatives at the element interfaces even when the Hamiltonian is discontinuous. Our method, while effective for a Cartesian grid, can not handle complex geometries. The next step is to deal with different types of boundary conditions and apply Hermite methods to curvilinear coordinate systems. We believe that sensing on a curvilinear coordinate system will be a straightforward generalization since we can map the curvilinear element onto the reference element on the unit square.

6 Declarations

6.1 Funding

Allen Alvarez Loya was funded by NSF Grant DGE-1650115. Daniel Appelö was supported, in part, by NSF Grant DMS-1913076.

6.2 Conflicts of interest/Competing interests

On behalf of all authors, the corresponding author states that there is no conflict of interest

6.3 Availability of data and material

All data generated or analysed during this study are included in this published article.

6.4 Code availability

The code used to generate the results in this work is available upon request to Allen (allen.alvarezloya@colorado.edu).

6.5 Authors' contributions

N/A.

6.6 Ethics Approval

N/A.

6.7 Consent to Participate

N/A.

6.8 Consent to Publication

N/A.

References

1. Daniel Appellö, Thomas Hagstrom, and Arturo Vargas. Hermite methods for the scalar wave equation. *SIAM Journal on Scientific Computing*, 40(6):A3902–A3927, 2018.
2. Xi Ronald Chen, Daniel Appellö, and Thomas Hagstrom. A hybrid Hermite–discontinuous Galerkin method for hyperbolic systems with application to Maxwell’s equations. *Journal of Computational Physics*, 257:501–520, 2014.
3. Yingda Cheng and Chi-Wang Shu. A discontinuous Galerkin finite element method for directly solving the Hamilton–Jacobi equations. *Journal of Computational Physics*, 223(1):398–415, 2007.
4. Yingda Cheng and Zixuan Wang. A new discontinuous Galerkin finite element method for directly solving the Hamilton–Jacobi equations. *Journal of Computational Physics*, 268:134–153, 2014.
5. Michael G Crandall, Lawrence C Evans, and P-L Lions. Some properties of viscosity solutions of Hamilton-Jacobi equations. *Transactions of the American Mathematical Society*, 282(2):487–502, 1984.
6. Michael G Crandall and P-L Lions. Two approximations of solutions of Hamilton-Jacobi equations. *Mathematics of computation*, 43(167):1–19, 1984.
7. Michael G Crandall and Pierre-Louis Lions. Viscosity solutions of Hamilton-Jacobi equations. *Transactions of the American mathematical society*, 277(1):1–42, 1983.
8. Michael G Crandall and Andrew Majda. Monotone difference approximations for scalar conservation laws. *Mathematics of Computation*, 34(149):1–21, 1980.
9. John Goodrich, Thomas Hagstrom, and Jens Lorenz. Hermite methods for hyperbolic initial-boundary value problems. *Mathematics of computation*, 75(254):595–630, 2006.
10. Jean-Luc Guermond and Richard Pasquetti. Entropy-based nonlinear viscosity for fourier approximations of conservation laws. *Comptes Rendus Mathematique*, 346(13–14):801–806, 2008.
11. T. Hagstrom and D. Appellö. Experiments with Hermite methods for simulating compressible flows: Runge-Kutta time-stepping and absorbing layers. In *13th AIAA/CEAS Aeroacoustics Conference*, number 2007-3505, 2007.
12. Thomas Hagstrom and Daniel Appellö. Solving PDEs with Hermite Interpolation. In *Spectral and high order methods for partial differential equations ICOSAHOM 2014*, pages 31–49. Springer, 2015.
13. Ami Harten and James M Hyman. Self adjusting grid methods for one-dimensional hyperbolic conservation laws. *Journal of computational physics*, 50(2):235–269, 1983.
14. Guang-Shan Jiang and Danping Peng. Weighted ENO schemes for Hamilton–Jacobi equations. *SIAM Journal on Scientific computing*, 21(6):2126–2143, 2000.
15. Andreas Klöckner, Tim Warburton, and Jan S Hesthaven. Viscous shock capturing in a time-explicit discontinuous Galerkin method. *Mathematical Modelling of Natural Phenomena*, 6(3):57–83, 2011.
16. A. Kornelus and D. Appellö. Flux-conservative Hermite methods for simulation of nonlinear conservation laws with shocks. *J. of Sci. Comput.*, 76:24–47, 2018.
17. Richard D Neidinger. Efficient recurrence relations for univariate and multivariate Taylor series coefficients. In *Conference Publications*, volume 2013, page 587. American Institute of Mathematical Sciences, 2013.
18. Stanley Osher and Chi-Wang Shu. High-order essentially nonoscillatory schemes for Hamilton–Jacobi equations. *SIAM Journal on numerical analysis*, 28(4):907–922, 1991.
19. Per-Olof Persson and Jaime Peraire. Sub-cell shock capturing for discontinuous Galerkin methods. In *44th AIAA Aerospace Sciences Meeting and Exhibit*, page 112, 2006.
20. Jianxian Qiu. Hermite WENO schemes with Lax-Wendroff type time discretizations for Hamilton-Jacobi equations. *Journal of Computational Mathematics*, pages 131–144, 2007.
21. Jianxian Qiu and Chi-Wang Shu. Hermite WENO schemes for Hamilton–Jacobi equations. *Journal of Computational Physics*, 204(1):82–99, 2005.
22. Panagiotis E Souganidis. Approximation schemes for viscosity solutions of Hamilton-Jacobi equations. *Journal of differential equations*, 59(1):1–43, 1985.

-
23. Zhanjing Tao, Fengyan Li, and Jianxian Qiu. High-order central hermite weno schemes on staggered meshes for hyperbolic conservation laws. *Journal of Computational Physics*, 281:148–176, 2015.
 24. Yousef Hashem Zahran and Amr H Abdalla. Seventh order Hermite WENO scheme for hyperbolic conservation laws. *Computers & Fluids*, 131:66–80, 2016.
 25. Yong-Tao Zhang and Chi-Wang Shu. High-Order WENO Schemes for Hamilton–Jacobi Equations on Triangular Meshes. *SIAM Journal on Scientific Computing*, 24(3):1005–1030, 2003.
 26. Feng Zheng, Chi-Wang Shu, and Jianxian Qiu. Finite difference Hermite WENO schemes for the Hamilton–Jacobi equations. *Journal of Computational Physics*, 337:27–41, 2017.